Title

Structures and Electronic Properties of Domain Walls in BiFeO3 Thin Films

Journal

National Science Review, 6(4)

ISSN

2095-5138

Authors

Huyan, Huaixun

Li, Linze

Addiego, Christopher

et al.

Publication Date

2019-07-01

DOI

10.1093/nsr/nwz101

REVIEW

National Science Review
6: 669–683, 2019
doi: 10.1093/nsr/nwz101
Advance access publication 27 July 2019

MATERIALS SCIENCE

Special Topic: Multiferroic Physics and Materials

Structures and electronic properties of domain walls in $BiFeO_3$ thin films

Huaixun Huyan[1,†], Linze Li[1,†], Christopher Addiego[2], Wenpei Gao[1] and Xiaoqing Pan[1,2,3,*]

ABSTRACT

Domain walls (DWs) in ferroelectrics are atomically sharp and can be created, erased, and reconfigured within the same physical volume of ferroelectric matrix by external electric fields. They possess a myriad of novel properties and functionalities that are absent in the bulk of the domains, and thus could become an essential element in next-generation nanodevices based on ferroelectrics. The knowledge about the structure and properties of ferroelectric DWs not only advances the fundamental understanding of ferroelectrics, but also provides guidance for the design of ferroelectric-based devices. In this article, we provide a review of structures and properties of DWs in one of the most widely studied ferroelectric systems, $BiFeO_3$ thin films. We correlate their conductivity and photovoltaic properties to the atomic-scale structure and dynamic behaviors of DWs.

Keywords: domain wall, $BiFeO_3$, ferroelectric, conductivity, photovoltaics, thin film

[1]Department of Materials Science and Engineering, University of California, Irvine, CA 92697, USA; [2]Department of Physics and Astronomy, University of California, Irvine, CA 92697, USA and [3]Irvine Materials Research Institute, University of California, Irvine, CA 92697, USA

*__Corresponding author__. E-mail: xiaoqinp@uci.edu
†Equally contributed to this work.

Received 14 April 2019; **Revised** 12 July 2019; **Accepted** 14 July 2019

INTRODUCTION

Since the discovery of ferroelectricity in $BaTiO_3$ in the mid 1940s [1], ferroelectric oxides have become a prototypical example of functional materials, attracting considerable interest both in fundamental research and device engineering. The spontaneous polarization in a ferroelectric can be reversed through the application of an external electric field that is greater than the coercive field, a behavior similar to the reorientation of magnetic moments under an applied magnetic field for ferromagnetic materials. Due to such switchability and the small size of ferroelectric domains, which can be as small as a few nanometers [2], ferroelectric materials can be utilized in an important class of high-density and non-volatile memories. Ferroelectric memories have a number of advantages, such as low power consumption, fast writing speed, and high cyclability, which, in most cases, is superior to the performance of other non-volatile devices [3].

The domain wall (DW) is an important element of ferroelectric materials. It is a quasi-2D boundary separating domains that differ in the orientation of spontaneous polarizations. The DW types are distinguished by the rotation angles of polarization between neighboring domains, e.g. 71°, 109°, and 180° in $BiFeO_3$. DWs appear as the material is cooled below the Curie temperature (T_C) [4]. This occurs as a result of symmetry breaking in the crystal structure during the phase transition, and the domain pattern that forms is governed by minimization of the free energy of the boundaries [5,6]. This free energy is related to electrostatic energy and elastic energy, which can be affected by several factors. Polarization bound charges and free charges [7–10] affect electrostatic energy, misfit strain contributes to elastic energy [10], and defects [11–14] affect both electrostatic and elastic energy. Variation of these factors can lead to the stabilization of a number of unique DW structures, either ordered or disordered. Over the past few years, there has been continuously increasing evidence showing that DWs can exhibit novel properties, including enhanced conductivity [15–19], photovoltages [20–26] and current rectification [27], all of which make DWs appealing for applications as active elements in future nanodevices.

In this review, we summarize the recent progress on the experimental study of DW structures and properties in one of the most widely studied ferroelectric systems, $BiFeO_3$. We will first illustrate the microstructure of 71°, 109° and 180° DWs in $BiFeO_3$ thin films, and the engineering methods used to produce ordered DW patterns, including boundary-condition engineering and defect engineering. The microstructures and atomic structures of DWs are revealed by a combination of piezoresponse force microscopy (PFM), aberration-corrected atomic-resolution scanning transmission electron microscopy (STEM), and *in situ* transmission electron microscopy (TEM). This is followed by a discussion on the properties of the DWs including DW conductivity and DW photovoltaics. The studies on DW conductivity include those findings from uncharged and charged DWs, and the formation of charged domain walls (CDWs) controlled by an external electric field. We will then show that characterization of the microstructure can provide us with a fundamental understanding of the properties at the macro scale and associated structural mechanisms. Finally, we will discuss the new possibilities brought by the recent advancement of electron microscopy techniques including high-energy-resolution electron energy loss spectroscopy (EELS) and multi-dimensional imaging, on the study of the electronic structure, charge and their interplay at the ferroelectric DWs and ferroelectric materials in general.

DW STRUCTURES AND BOUNDARY-CONDITION ENGINEERING OF DW PATTERNS

$BiFeO_3$ bulk material has a rhombohedral structure consisting of two pseudocubic (P) perovskite unit cells connected along the body diagonal with the two oxygen octahedra rotated clockwise and counterclockwise around the axis by 13.8° [28]. $BiFeO_3$ thin films with misfit strain less than 4.5% [29] exhibit a monoclinically distorted structure that is similar to the bulk rhombohedral phase, and are thus referred to as '*rhombohedral*-like (R-like)' structures [30], as shown in Fig. 1a [31]. In pseudocubic unit cells of the R-like structure, the oxygen octahedra and the central Fe cation are displaced from their respective positions at the face and body centers, giving rise to a large spontaneous polarization (~100 $\mu C\ cm^{-2}$) along the $<111>_P$ (subscripts P denote pseudocubic indices) directions, and resulting in four different ferroelastic variants (r_1–r_4) (Fig. 1b) [32]. Rotations between polarization variants in the R-like $BiFeO_3$ can be 71° (ferroelastic–ferroelectric), 109° (ferroelastic–ferroelectric), or 180° (ferroelectric), yielding three types of domain walls. When the misfit strain is larger than 4.5%, the $BiFeO_3$ unit cell will transform into a '*tetragonal*-like (T-like)' structure [30], as shown in Fig. 1a. In such a structure, the Fe atom is coordinated by five oxygen atoms and displaced from the body center, resulting in a giant polarization of ~ 150 $\mu C/cm^2$ [33].

Thanks to the recent advances in atomic-level control of thin-film growth techniques, high-quality ferroelectric thin-film epitaxial growth can now be achieved with precise control over composition, interfaces, and defect introduction [34–39]. The ability to synthesize high-quality films has enabled a steady growth in the atomic-level study of the physical [31,40,41] and electrical properties [14–21,42] of ferroelectric materials.

In ferroelectric and ferroelastic thin films, patterns of DWs depend strongly on the boundary conditions at the surfaces or interfaces. First, the lattice mismatch between the film and substrate leads to a biaxial-strain mechanical boundary condition [37,43–45], which can be altered by choosing substrates spanning a wide range of lattice parameters [29,32,46–48]. Second, the electrical boundary condition is critically dependent on free charge compensation at the interfaces and can be tailored by choosing substrates or epitaxial buffer layers with different conductivities [49–51]. Additional restrictions on the boundary condition can be made by changing the vicinality or atomic termination of the substrates [52,53]. By modifying these boundary conditions, previous experimental studies demonstrated the capability to fabricate different types of ordered DW patterns (i.e. 109°, 71°, and 180° DWs) in $BiFeO_3$ thin films (Fig. 1c, d and e) [22,42,54].

71° and 109° domain walls

Synthesis of epitaxial $BiFeO_3$ thin films containing periodically ordered patterns of 71° and 109° DWs on a $SrRuO_3$ layer on orthorhombic $DyScO_3$ substrate was reported by Chu *et al.* in 2006 [5]. By careful control of the growth for the $SrRuO_3$ layer, the in-plane lattice parameters of $SrRuO_3$ films are pinned by the $DyScO_3$ substrate. Consequently, the in-plane lattice parameters of $BiFeO_3$ films are also pinned by the $DyScO_3$ substrate and such constraints imposed by the orthorhombic substrate result in the stabilization of periodic twinning domain patterns in the $BiFeO_3$ films. The observed domain patterns develop along either the $[100]_P$ or $[101]_P$ direction [4], which correspond to 109° or 71° DWs, respectively. In Chu's follow-up works [52,55], it was demonstrated that the type of DWs

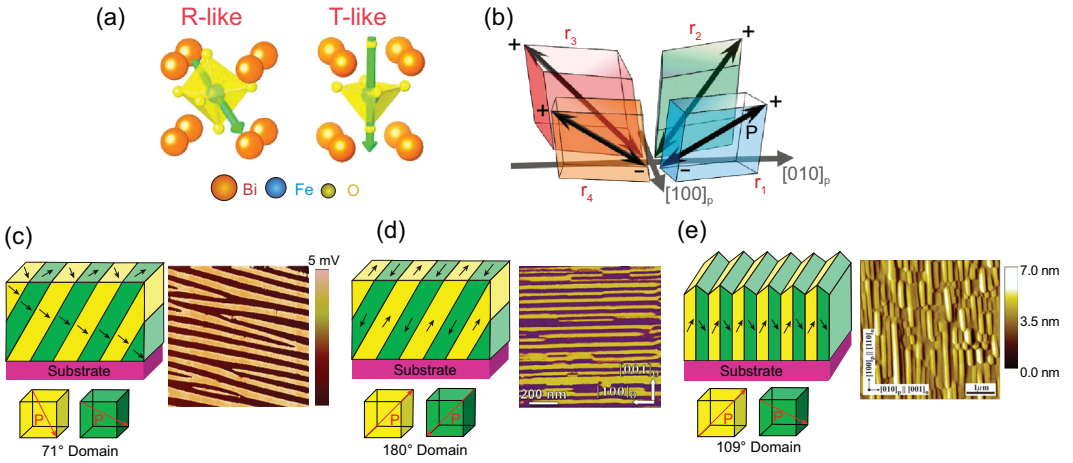

Figure 1. a) Atomic models of R-like and T-like unit cell structures in $BiFeO_3$. Reprinted with permission from Li *et al.* [31]. Copyright (2017) American Chemical Society. b) Four variants of the $BiFeO_3$ pseudocubic unit cell. Reprinted with permission from Nelson *et al.* [32]. Copyright (2011) American Chemical Society. c), d) and e) are schematics of different DWs with corresponding in-plane PFM phase mappings: periodic domain patterns of c) 71°, reprinted with permission from Bhatnagar *et al.* [22]. Copyright (2013) Springer Nature; d) 180°, reprinted with permission from Chen *et al.* [42]. Copyright (2015) American Chemical Society; e) 109°, reprinted with permission from Folkman *et al.* [54]. Copyright (2009) AIP Publishing.

in the as-grown 100-nm-thick $BiFeO_3$ films can be controlled by varying the thickness of an $SrRuO_3$ conducting buffer layer between the ferroelectric and the substrate. PFM measurements show that the 109° DWs are dominant when the $SrRuO_3$ thickness is less than 5 nm; DWs are a mixture of 109° and 71° when the $SrRuO_3$ thickness is between 5 and 25 nm; and only 71° DWs exist when the $SrRuO_3$ thickness is above 25 nm. The underlying mechanism can be attributed to the interaction of the polarization bound charge at the interface and free charge carriers in the $SrRuO_3$ electrode. In particular, the 71° domain structures have a single out-of-plane polarization vector resulting in uniform positive and negative bound charge on opposite surfaces of the film. This bound charge can produce a large depolarization field, which would destabilize the domain structure unless it can be screened by free charge carriers. It follows that the 71° domain structures are usually stabilized in $BiFeO_3$ thin films with the insertion of thick (>25 nm) bottom electrodes [55–57]. In contrast, if the surfaces of $BiFeO_3$ thin films are uncompensated by free charges, the system favors the formation of 109° DW° patterns with alternating out-of-plane polarization that can reduce the total electrostatic energy.

180° domain walls

The observation of periodically ordered 180° DWs in $BiFeO_3$ thin film was reported by Chen *et al.* in 2015 [42], where they studied 32-nm-thick epitaxial $(110)_P$ $BiFeO_3$ thin films grown on orthorhombic $GdScO_3$ $(010)_o$ (subscripts o denote orthorhombic indices) substrate. Based on PFM measurements, the structures are composed of periodic stripe domains separated by 180° DWs that locate at $(11\bar{2})$ and intersect with the film surface along the $[100]_P$ direction. Their results also show that, as the film thickness increases to 70 nm, 71° DWs become dominant. The domain pattern formation strongly depends on the elastic and electrostatic boundary conditions. The depolarization field, which corresponds to electrostatic energy, is inversely proportional to the film thickness and can be compensated by free charges from conducting electrodes. In Chen's work, the $BiFeO_3$ was directly grown on insulating $GdScO_3$ substrate with insufficient free charges to fully compensate the depolarization field. In thinner films, like the 32-nm-thick film, 180° domain patterns with alternating out-of-plane polarization are formed to reduce the electrostatic energy dominated by the depolarization field. The 180° domains, however, are non-ferroelastic and could not release the strain imposed by the substrate. When the film thickness increases to 70 nm, the depolarization field is reduced; meanwhile the elastic effects start to dominate, resulting in the formation of 71° ferroelastic domains to reduce the elastic energy of the system [52,58,59].

Vortex domains

Beyond the regular domain structures mentioned above, Nelson *et al.* reported the existence of arrays of spontaneous vortex domains in a 20-nm-thick $(001)_P$ $BiFeO_3$ thin film on $(110)_o$ $TbScO_3$

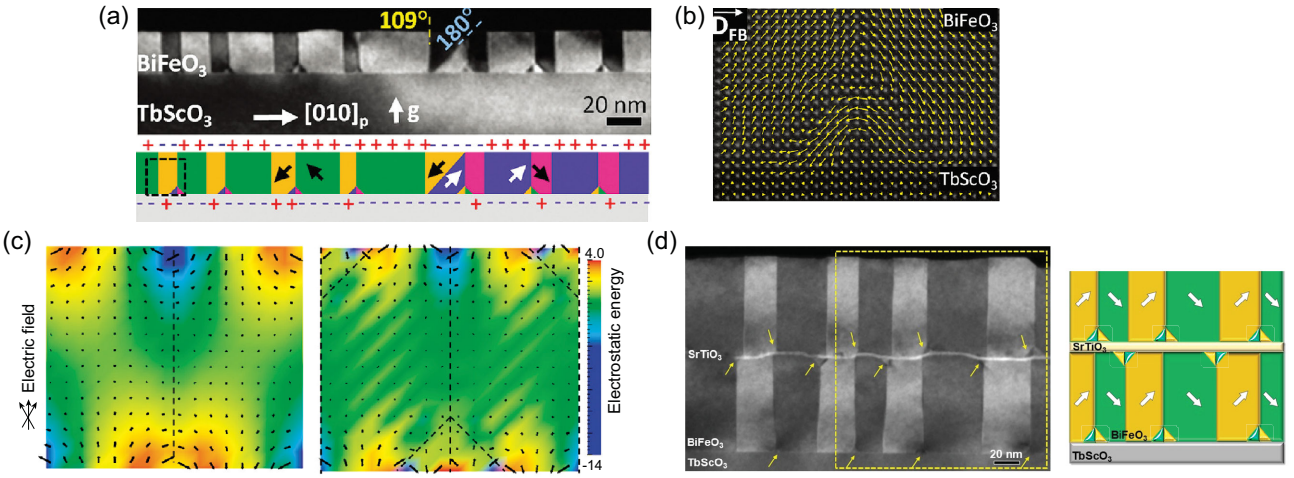

Figure 2. a) Dark-field TEM and corresponding schematic. b) Polarization mapping of 109° DWs that form a vortex domain. c) Vector plots of depolarization field overlaid with electrostatic energy mapping with (right) or without (left) vortex domains. Reprinted with permission from Nelson *et al.* [32]. Copyright (2011) American Chemical Society. d) Dark-field TEM image of domain pattern in a $BiFeO_3/SrTiO_3/BiFeO_3$ tri-layer structure grown on $TbScO_3$ substrate, and corresponding schematic of the highlighted region.

substrate in 2011 [32]. The cross-sectional TEM image and the corresponding schematic in Fig. 2 show the existence of triangle domains at the $BiFeO_3/TbScO_3$ interface where the 109° DWs terminate. Polarization mapping at the triangle domain reveals the formation of a 'mirrored pair' of inclined 180° DWs, resulting in a closure vortex structure with polarization rotating around the 109° and 180° DW intersection point. Such a structure is formed due to the existence of bound charge density waves, i.e. alternate positive and negative bound charges at the interfaces, which produce a non-uniform depolarization field (Fig. 2c) favoring the vortex formation. According to our experimental results shown in Fig. 2d, vortex arrays can also be realized at both $BiFeO_3/SrTiO_3$ and the $BiFeO_3/TbScO_3$ interfaces in a $BiFeO_3/SrTiO_3/BiFeO_3$ heterostructure grown on the (110) $TbScO_3$ substrate. Vortex structures were also discovered recently in $PdTiO_3$ thin films [60–62] and $PdTiO_3/SrTiO_3$ superlattices [36]. The periodicity of the vortices can be tuned by growing the $PbTiO_3$ films with different thicknesses [60]. In ultrathin $PbTiO_3$ layers embedded in the $PbTiO_3/SrTiO_3$ superlattices, long-range ordered vortex–antivortex arrays were found to exhibit a nearly continuous polarization rotation [36]. It is interesting to note that as the thickness of the $BiFeO_3$ layer decreases, the vortices at the bottom and top interfaces of each $BiFeO_3$ layer will move closer to each other. As a result, one can expect to observe an array of new vortices (formed by the merging of the abovementioned vortices located at the bottom and top interfaces) in each $BiFeO_3$ layer of the $BiFeO_3/SrTiO_3$ or $BiFeO_3/TbScO_3$ superlattices, similar to the vortex arrays observed in the $PbTiO_3/SrTiO_3$ superlattices.

DEFECT ENGINEERING

While boundary-condition engineering has demonstrated tremendous success in control of DW patterns in ferroelectric thin films, one major limitation of such a method has been that once the variable at the boundary condition is set, such as the choice of substrate, further modification to control or alter DW patterns during material synthesis becomes difficult. This reduces the parameter space for creating more complex structures with ordered DW patterns and thus imposes restrictions on the functionalities of the system. On the other hand, defects in ferroelectric oxides can also have a remarkable impact on ferroelectric domain structures. Commonly observed defects such as dislocations and vacancies can interact with domains and DWs to pin polarization configurations. The recent work by Li *et al.* [31,40,41] and others [35] reported a strong electrostatic driving force provided by charged impurity defects, another type of common defect with a structure different from the host material. Their results suggested the possibility of using engineered impurity defects in combination with suitable interface boundary conditions to control domain formation and create complex DW structures.

Planar defects

Li *et al.* initially discovered an array of nanoscale planar charged defect that were accidentally introduced

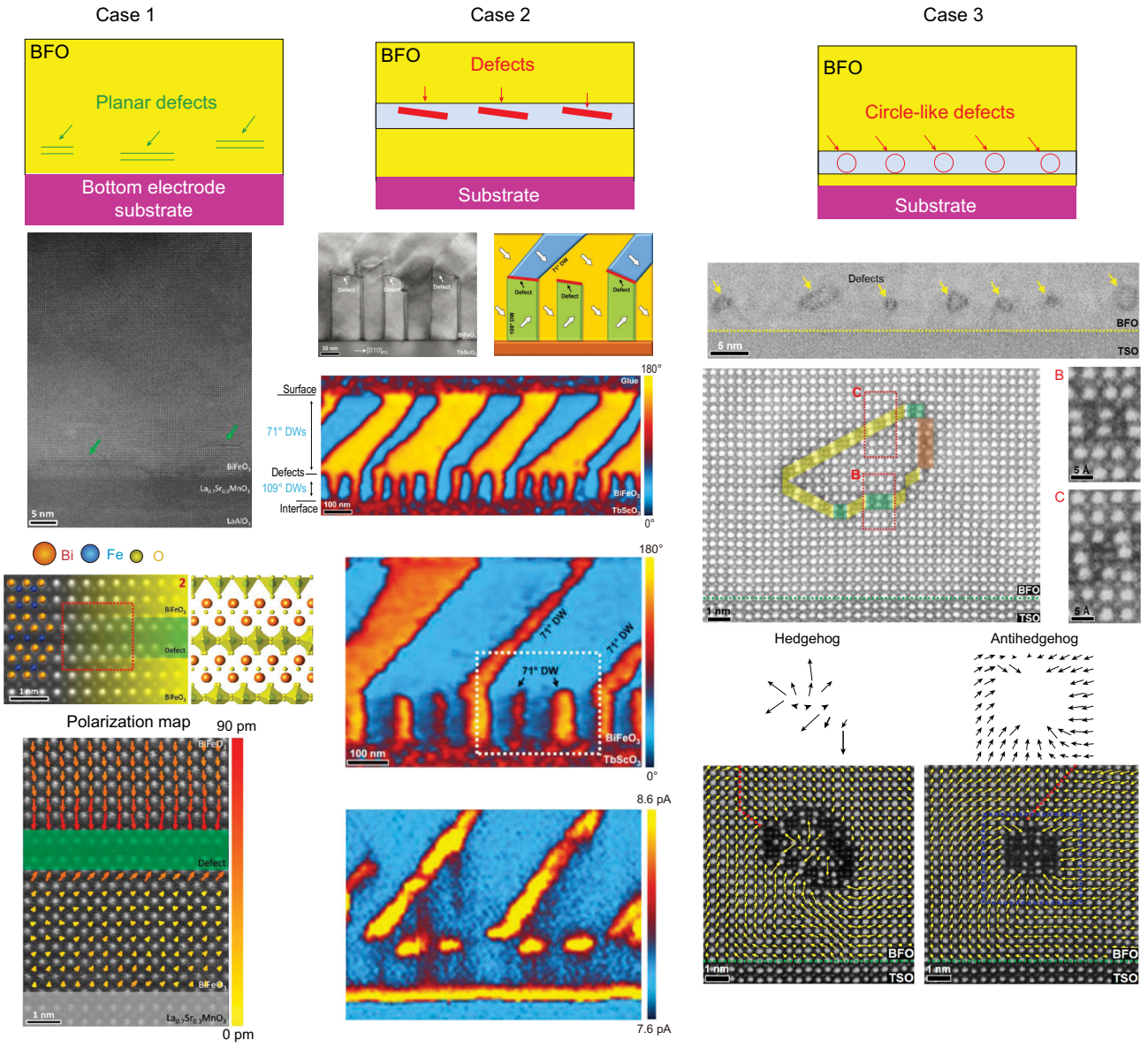

Figure 3. Case 1 shows a planar defect with STEM images and polarization mapping. Reprinted with permission from Li *et al.* [31]. Copyright (2017) American Chemical Society. Case 2 represents circle-like defects with polarization mapping and corresponding defect-region magnified maps. Reprinted with permission from Li *et al.* [40]. Copyright (2017) WILEY-VCH Verlag GmbH & Co. KGaA, Weinheim. Case 3 shows linear defects with TEM and PFM phase images. Reprinted with permission from Li *et al.* [41]. Copyright (2018) American Physical Society.

during the synthesis of a $BiFeO_3$ film, which can induce a novel mixed-phase 'head-to-head' polarization structure [31]. In Fig. 3 case 1, the high-angle annular dark-field (HAADF) image shows brighter and darker dots representing Bi and Fe columns, respectively. Around the defect region Bi_2FeO_{6-x} formed, consisting of one layer of FeO_6 octahedra sandwiched by two Bi_2O_2 layers. The defect is a few atomic layers thick and is well aligned along the film growth direction. Polarization mapping of the defect region shows head-to-head polarization at the planar defect region. The region above the planar defect has a T-like structure with polarization downward along $[00\bar{1}]_P$, while the region below has R-like structure with opposing polarization upward along the unit cell diagonal. This upward polarization does not follow the overall downward built-in field that is induced by Schottky contact of $BiFeO_3/La_{0.7}Sr_{0.3}MnO_3$ [32], indicating the existence of another built-in field pointing upward caused by the defect.

Linear defects

Inspired by the above finding, Li *et al.* demonstrated a route to deliberately creating an array of linear

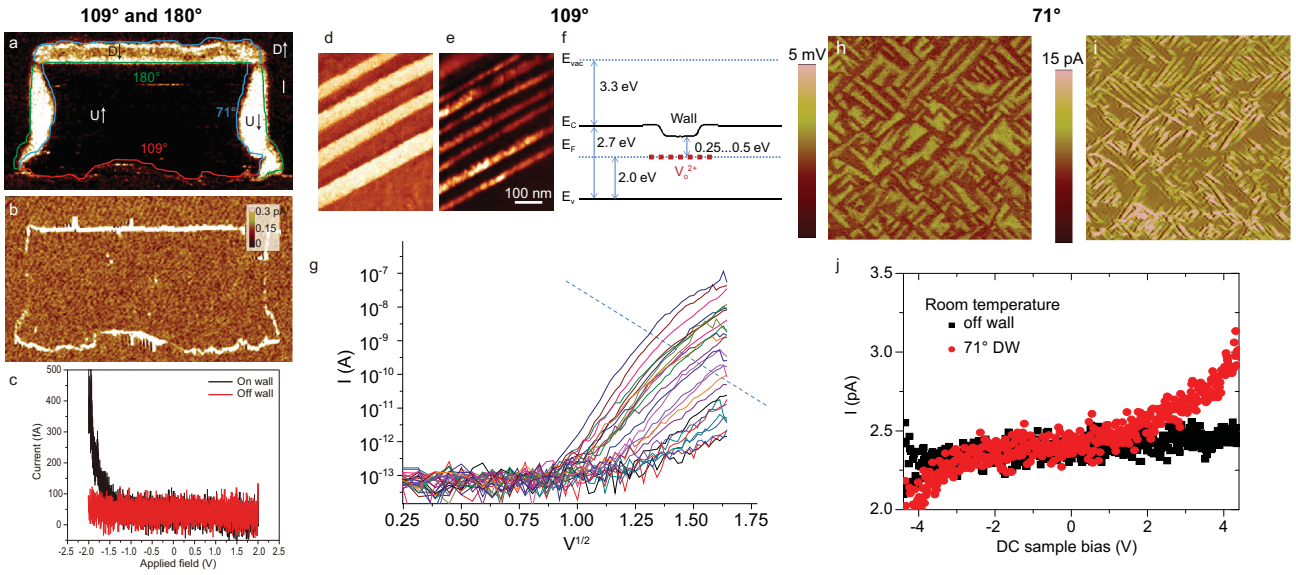

Figure 4. a) In-plane PFM image showing 71° (blue), 109° (red) and 180° (green) DWs. b) Corresponding c-AFM image. c) *I–V* curves taken on the DW (black) and off the DW (red). Reprinted with permission from Seidel *et al.* [15]. Copyright (2009) Springer Nature. d) and e) are PFM phase and c-AFM images of 109° strip domains respectively. f) Schematic band structure of 109° DW. g) *I–V* curves of 109° DW. Reprinted with permission from Seidel *et al.* [16]. Copyright (2010) American Physical Society. h) and i) are PFM phase and c-AFM images of 71° domains. j) *I–V* curves taken on the 71° DW (red) and off the DW (black). Reprinted with permission from Farokhipoor *et al.* [17]. Copyright (2011) American Physical Society.

charged defects in the $BiFeO_3$ matrix to configure special DW patterns that are not favorable in natural boundary conditions [40]. By slightly changing the substrate temperature during the film growth, an array of linear charged Fe-rich defects can be introduced into the $BiFeO_3$ film at a constant level that is 110–130 nm above the interface (Fig. 3 case 2). The interaction between the charged defects and the polarization lead to a reconfigured DW pattern in the $BiFeO_3$ film. As shown in Fig. 3 case 2, a linear defect is observed on each 109° domain that is polarized upward (green) and the horizontal dimension of the defect matches the domain width exactly. Above some of the defects, 71° domains (blue) are stabilized with the DWs located in the $(01\bar{1})_P$ planes, which are different from the $(101)_P$-oriented 71° domain stripes previously reported in $BiFeO_3$ thin films grown on orthorhombic substrates. In contrast, the downward polarized domains (yellow) in the lower portion of the film are not blocked by the defects and can extend their volume to the upper portion. As a result, a transformation from 109° to 71° DW patterns across the defects is observed, as well as an array of 'head-to-head' positively charged DWs located exactly at the negatively charged defects. Periodic ordering of these DW patterns is further confirmed by a PFM image of the same heterostructure in the cross section, in which the defects are not resolvable. The PFM image also shows a large 71° domain on top of five 109° domains, with the defects lying in between. The conductivity mapping of the same area was measured and shows the enhanced conductivity of the 71° DWs.

Circle-like defects

In addition to the planar and linear defects, Li *et al.* found that circle-like defects, named non-stoichiometric nanoregions (NSNRs), can stabilize hedgehog or antihedgehog nanodomains [41]. The circle-like defects were deliberately introduced by changing the substrate temperature during the film growth, similar to the previous example. The stabilized hedgehog/antihedgehog domains can be coupled with polarization rotations, which results in polarization vortices. The hedgehog and antihedgehog domains are shown in Fig. 3 case 3. The formation of the domains is based on non-stoichiometric planar units and stepped units as shown in B and C, respectively, with excess oxygen and result in local negative net charge. The region circled by the defect is a hedgehog domain with a diameter of 4 unit cells in length. The antihedgehog domains with continuous polarization rotation are formed in the region right outside the defect circle and result in flux-closure vortex structure on a large scale.

DOMAIN WALL CONDUCTIVITY

109° and 180° domain walls

Seidel *et al.* reported DW conductivity in 2009 [15]. Figure 4a shows the PFM in-plane images of

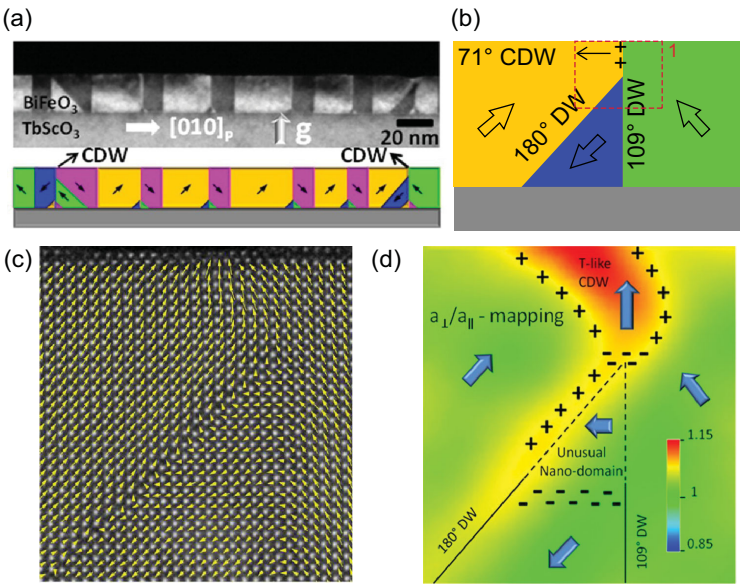

Figure 5. a) Cross-sectional dark-field TEM image showing $BiFeO_3$ domain structure. b) CDW region. c) Polarization mapping of a similar area of b). d) Corresponding $a_{\perp}/a_{\parallel}$ mapping. Reprinted with permission from Li *et al.* [56]. Copyright (2013) American Chemical Society.

100-nm-thick $BiFeO_3$ thin film on $SrRuO_3$ bottom electrode on $SrTiO_3$ substrate with a region where 71°, 109° and 180° DWs have been written. The conducting atomic force microscopy (c-AFM) image (Fig. 4b) taken in the same region indicates enhanced electrical conduction at 109° and 180° DWs but not at 71° DWs. The current–voltage (*I*–*V*) curves (Fig. 4c) are measured at the 180° DW or at the middle of the nearby domain region. The black curve reveals that DW has activated conduction while the red curve shows that the domain region has less conduction. They then specifically studied 109° DW conductivity in 2010 [16]. They used 100-nm-thick 10% La-doped $BiFeO_3$ thin film, in which La doping allows coherent 109° domain growth [55], with an $SrRuO_3$ bottom electrode grown on $(110)_o$ $DyScO_3$ substrate. PFM and c-AFM results (Fig. 4d and e) indicate an ordered 109° stripe domain structure and corresponding local conductivity at the DWs. The *I*–*V* curves (Fig. 4g) are measured by using AFM tip stepping perpendicular to the 109° DW with the same load. The *I*–*V* curves increase linearly at low voltage and transit to large curvature at higher voltage. Such phenomena were explained by the oxygen vacancy activation in an electric field as shown schematically in Fig. 4f, where enhanced conductivity at the wall is caused by changes in the local bandgap [55].

71° domain wall

Although in Seidel *et al.*'s work the conductivity of the 71° DW was not found, Farokhipoor *et al.* reported 71° DW conductivity in 2011 [17]. They studied 40–70-nm-thick $BiFeO_3$ thin films with $SrRuO_3$ bottom electrode on $SrTiO_3$ substrate. The in-plane PFM results (Fig. 4h and i) show that most of the DWs observed are 71° DWs with enhanced conduction. The *I*–*V* curves (Fig. 4j) are measured in constant polarization regions and in regions containing a 71° domain wall. The DW *I*–*V* curve shape (in red in Fig. 4j) reveals a Schottky emission mechanism with the majority of carriers provided by oxygen vacancies. The observed conductivity at 71° DWs here is different from the previous study by Seidel *et al.*, where the 71° DW conductivity is not found in $BiFeO_3$ films that were grown on $DyScO_3$ substrates at higher deposition rates and with higher oxygen pressure [15]. Such differences indicate that the material synthesis conditions are critical for the conductive nature of different types of DWs.

Charged domain wall

In ferroelectrics, most DWs are charge-neutral as a result of 'head-to-tail' polarization configurations, such as in the previous examples. The electrostatic energy of uncharged DWs is usually minimized but they only have low conductivity that is thermally activated [57]. In contrast, DWs with polarization discontinuity carry net bound charge and are referred to as charged domain walls (CDWs). They are electrically active and can possess much higher conductivity than the charge-neutral DWs. There are two types of CDWs in ferroelectrics. One is formed where the original charge-neutral DW is bent by external applied fields of internal defect pinning effects. Such CDWs have conductivities of ~ 10–10^3 times as high as those of bulk domains [7] but tend to reduce to an uncharged state when the applied field is removed or the pinning effects are thermally overcome [63]. The other type is directly formed by 'head-to-head' or 'tail-to-tail' polarization configuration and can be stabilized by free charge carrier compensation without applied fields or defect pinning [64–66]. These CDWs can have very high conductivity up to 10^9 times that of the bulk domains and result in an insulating-to-metallic transition [64,67]. Furthermore, the net bound charges can produce a depolarization field that results in an increased electromechanical response and thus better piezoelectric properties [68].

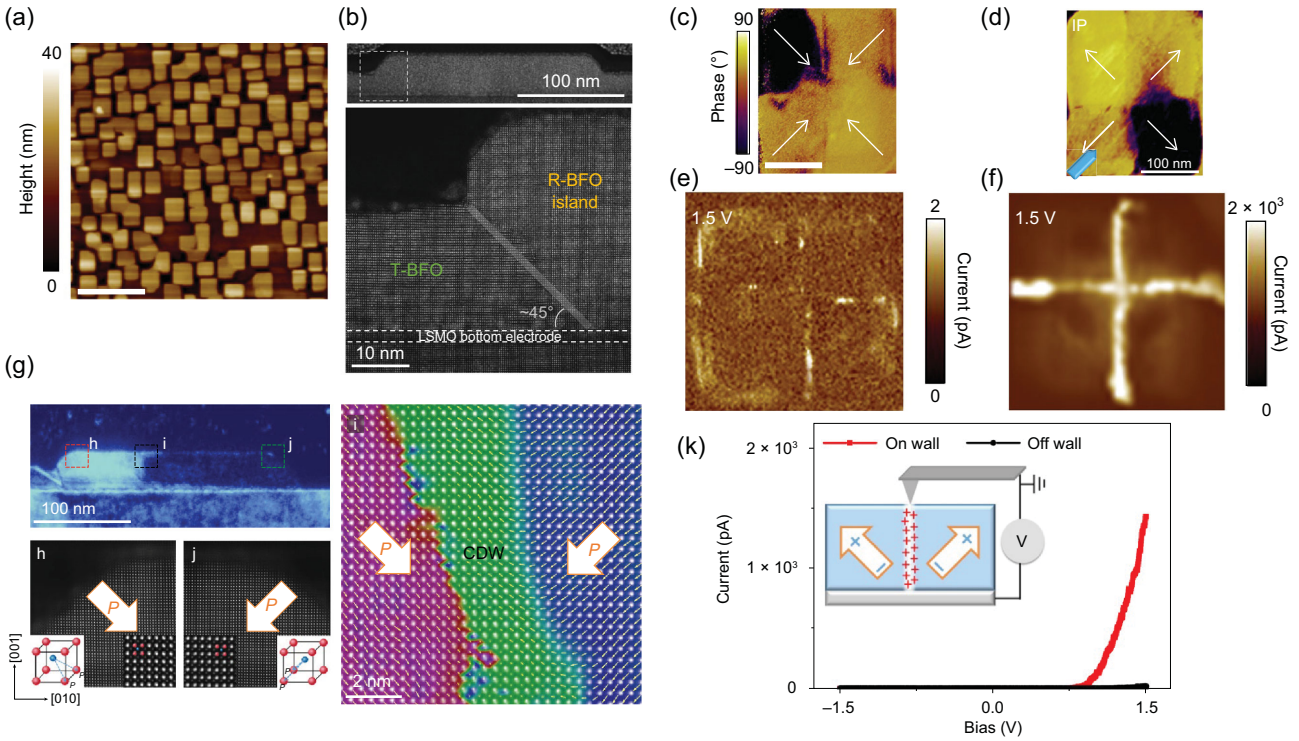

Figure 6. a) Topography of BFO (001) thin film with a self-assembled ordered nanoisland. b) Cross-sectional STEM image of the nanoisland. c) and d) are in-plane PFM images of 'head-to-head' and 'tail-to-tail' DW structures respectively, e) and f) are corresponding current maps. g) TEM image with enlarged regions h), i), and j). k) *I*–*V* curve of 'tail-to-tail' charged DW. Reprinted with permission from Ma *et al.* [69]. Copyright (2018) Springer Nature.

Charged domain wall attached to a triangle nanodomain

CDWs attached to triangle domains in $BiFeO_3$ film were reported by Li *et al.* [56]. They studied a 20-nm-thick $BiFeO_3$ film on a $(110)_o$ $TbScO_3$ substrate. The triangle domain structure, shown schematically in Fig. 5a, consists of vertical and inclined boundaries that are 109° and 180° DWs, respectively. The 71°CDW above the triangle domain shown in Fig. 5b region 1 is not a linear boundary but an area with gradual polarization rotations (Fig. 5c). Figure 5d shows a large $a_\perp/a_\parallel$ ratio at the 71°CDW, which indicates the formation of T-like structure at the CDW and a reduction of the electrostatic energy compared to that of a linear 'head-to-head' CDW. Also, the T-like 71°CDW region and the surrounding R-like regions result in both positive and compensating negative bound charges, which reduce the electrostatic energy even further.

Charged domain wall in a nanoisland

Ma *et al.* studied CDWs that form in square $BiFeO_3$ nanoislands. The film is grown on a 2-nm-thick (La, Sr)MnO_3 bottom electrode on (001) $LaAlO_3$ substrate [69]. As shown in Fig. 6a, their film is composed of a self-assembled, high-density array of square nanoislands. The low-magnification HAADF STEM image (Fig. 6b) shows that the nanoislands are 200 nm in length and 40 nm thick and grow from the 20-nm-thick $BiFeO_3$ matrix. High-magnification HAADF STEM images show clear boundaries between the R-like nanoislands and the T-like matrix. The in-plane polarization projection, measured with PFM (Fig. 6c), revealed that each nanoisland has four quadrants that have polarizations all pointing toward the island center. The out-of-plane polarization projection gives polarization pointing downward in the as-grown film. The dark-field TEM image show strong contrast between the left and right regions (Fig. 6g), suggesting different polarization directions. High-magnification HAADF STEM images of regions h, i, and j, highlighted in the low-magnification TEM image, each show different polarization states. Region h has polarization along the body diagonal towards the lower-right center and region j points to the lower-left center. Region i shows a 71° 'head-to-head' CDW with 3–5 nm width. Together, these results confirm that the nanoislands contain center-convergent quad-domains formed with 71°CDWs.

As shown in Fig. 6e and f, enhanced conductance with a cross-shape is observed by using c-AFM. Under 1.5 V, the 'head-to-head' CDW gives a maximum current of 2 pA. After the quad-domains are

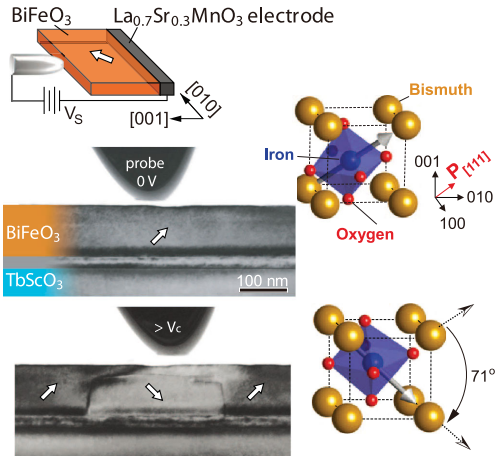

Figure 7. Cross-sectional TEM image of the $BiFeO_3$ thin films before and after switching, creating 71° DWs. Reprinted with permission from Nelson *et al.* [70]. Copyright (2011), American Association for the Advancement of Science.

switched to form a 'tail-to-tail' CDW, the maximum current measured reaches 2×10^3 pA. Such a huge difference between the two types of CDWs results from a difference in their interaction with the bottom electrode's free charge carriers. The free carriers in $La_{0.7}Sr_{0.3}MnO_3$ are p-type, which cannot interact with the positively charged 'head-to-head' DW but will accumulate at the negatively charged 'tail-to-tail' DW, resulting in very low conductance at 'head-to-head' CDWs and enhanced conductance at 'tail-to-tail' CDWs. The *I–V* curves show diode-type conductance, indicating a large current flow for forward bias, which results from the holes moving from the $BiFeO_3$ valence band to the tip. There is no obvious current detected for reverse bias since not enough holes can move to the $BiFeO_3$ valence band from the tip.

DOMAIN WALL DYNAMICS DURING DOMAIN SWITCHING

Regular thin film

$BiFeO_3$ domains can be easily switched by an external electric field, accompanied by DW creation or annihilation. The switching process shown in Fig. 7 was conducted by Nelson *et al.* using a 100 nm-thick $(001)_P$ $BiFeO_3$ with a 20 nm $La_{0.7}Sr_{0.3}MnO_3$ bottom electrode on $TbScO_3$ substrate [70]. The sample starts from a monodomain with polarization along $[111]_P$, then a portion of it is switched to a different polarization along $[11\bar{1}]_P$ by applying a 4 V bias, resulting in the formation of 71° DWs. However, this created domain did not reach the top surface but was pinned midway through the film, forming a horizontal 'tail-to-tail' CDW. This written domain can also be erased when applying a reversed bias. These switching processes open a path for properly writing or erasing CDWs.

Writing and erasing charged domain walls

With the understanding of the CDW formation and fundamental mechanisms, Crassous *et al.* reported a technique to easily write and erase CDWs in 45-nm-thick La-doped $BiFeO_3$ thin films with an $SrRuO_3$ bottom electrode on $(110)_o$ $DyScO_3$ substrate using PFM [9]. As the tip is moving along the $BiFeO_3$ surface, it creates a trailing field [71] that controls the in-plane polarization direction while the perpendicular electric field between the tip and bottom electrode controls the out-of-plane polarization direction, as shown in Fig. 8. Two 3×3 μm^2 regions were initially written into a monodomain with different trailing fields to demonstrate CDW writing. The writing process is initiated by applying an electric field to pull the out-of-plane polarization up combined with the trailing field to control the in-plane polarization direction. Domains 1, 2 and 3 are written first with the trailing field oriented along the $[001]_o$ direction and then domains 4, 5 and 6 are written with the trailing field along the opposite direction, so that domains 1–3 are polarized right and domains 4–6 are polarized left. The in-plane PFM results show 'head-to-head' CDWs at the 1/6, 2/5 and 3/4 interfaces, and 'tail-to-tail' CDWs at the 6/2 and 5/3 interfaces. The c-AFM mapping shows a current of ∼ 1.7 nA at the 'head-to-head' CDW with a 2.5 V bias applied. No conductance is detected at the 'tail-to-tail' CDW. Interestingly, such observations are totally different from the nanoisland CDW results reported by Ma *et al.* Crassous *et al.* believe that this is because the positive bound charges at the 'head-to-head' CDW are screened by the electrons from the tip and result in the creation of a conductive state. The 'tail-to-tail' CDW, on the other hand, has negative bound charges at the wall that cannot be compensated by the free electrons from the tip and therefore tend to minimize its charged density by forming zigzag DWs. Also, in Crassous *et al.*'s case, $SrRuO_3$ bottom electrodes (*n*-type) are used, providing mobile electrons to screen the positive bound charges at the 'head-to-head' CDWs, while Ma *et al.* used (La, Sr)MnO_3, which provides mobile holes, resulting in conducting 'tail-to-tail' CDWs as mentioned in section 'Charged domain wall in a nanoisland'.

The manipulation of CDWs through scanning probe microscopy (such as PFM) only allows access to the domain structure from the surface. Due to the requirement of free charge compensation, however, some CDWs present at the top surface of

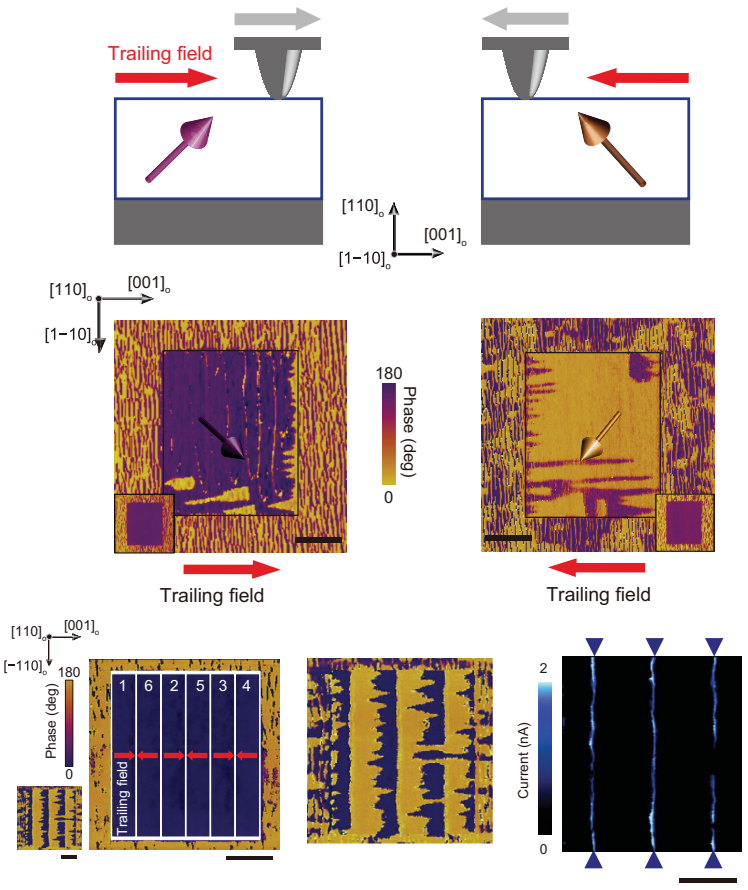

Figure 8. In-plane PFM phase and current mapping of $BiFeO_3$ thin films showing the writing of 'head-to-head' and 'tail-to-tail' charged DWs. Reprinted with permission from Crassous *et al.* [9]. Copyright (2015) Springer Nature.

ferroelectric films may not penetrate to the bottom interface. With cross-sectional *in situ* TEM, Li *et al.* reported a detailed study of local CDW writing and erasing in a 20-nm-thick $(001)_P$ $BiFeO_3$ thin film with an $La_{0.7}Sr_{0.3}MnO_3$ bottom electrode on $(110)_o$ $TbScO_3$ substrates [57]. The experimental set-up and writing process are schematically shown in Fig. 9a, with vertical 109° and inclined 180° DWs, and the corresponding cross-sectional dark-field TEM images are shown in the bottom row. In Fig. 9a, the left configuration is stable without CDW because the 109° and 180° DWs are far away from each other and therefore have very weak electrostatic interaction. Once the CDW has been written, the system is still stable since the bound charge close to the interface can be compensated by free carriers from the bottom electrode, reducing the electrostatic energy. The process was induced by applying an external electric field. The 109° and 180° DWs start to move as the bias reaches 1.7 V. While the bias is increasing, the two domains move toward each other and intersect, which eventually results in a shrinkage of the triangular domain and the formation of a CDW. The corresponding *I*–*V* curve in Fig. 9c reveals that the film has no conductivity below 3.5 V when there is no CDW, but passes 640 nA at 5.5 V once the CDW has formed. Such results give rise to the correlation between the enhanced conductance and the existence of CDW.

DOMAIN WALL PHOTOVOLTAICS

While the conventional light-to-electrical energy conversion process is achieved by using a *p*–*n* junction or a heterojunction [72,73] to separate electrons and holes, Yang *et al.* developed a new model for charge separation and photovoltage generation using $BiFeO_3$ ferroelectric DW modification under white light, yielding photovoltage significantly higher than the bandgap [20]. $BiFeO_3$ has a direct bandgap of ∼2.67 eV [74] with open-circuit voltage $V_{oc} \ll E_g$. The photovoltaic nanodevices are fabricated by defining two 500-μm-long platinum electrodes separated by 200 μm, on top of a100-nm-thick $BiFeO_3$ film; the electrodes can be either parallel or perpendicular to the DWs (Fig. 10a, b). Figure 10c, d shows the measured *I*–*V* curves of 71° DWs with both electrode configurations under no illumination and saturation illumination with white light. In the parallel configuration, V_{oc} is measured as 16 V with an in-plane short-circuit current density of $\sim 1.2 \times 10^{-4}$ A cm^{-2}. The perpendicular configuration, on the other hand, shows large photoconductivity but no V_{oc}. A drop in potential was measured across all types of DWs, with 180° DWs showing the largest drop, followed by 109° and then 71° DWs. They believe that such phenomena can be explained by the schematic band structure model in Fig. 10e depicting both the domains and DWs in dark conditions. The drop in potential across the DW creates an electric field that will provide an enhanced electron–hole pair separation process when illuminated. The separated electrons and holes build up on either side of the DWs and sum up over a large scale, leading to the large V_{oc}. In contrast, if the light is incident inside the domain, the excited charge is localized and tightly bound due to the weak built-in electrical field, resulting in a quick recombination and no photovoltaic effect.

This model, however, has been challenged by Bhatnagar *et al.*'s work with a measurement combing photoelectric AFM and PFM at the DWs and inside domains on 100 nm-thick $(001)_P$ $BiFeO_3$ thin films grown on $(110)_o$ $TbScO_3$ substrate [22]. They studied the $BiFeO_3$ photovoltaic effect on both 71° and 109° DWs, and the experimental set up is similar to the schematics in Fig. 11a with Pt electrodes that are 250 μm in length. The *I*–*V* curves of 109° DWs with parallel geometry give V_{oc} of 5.4 V,

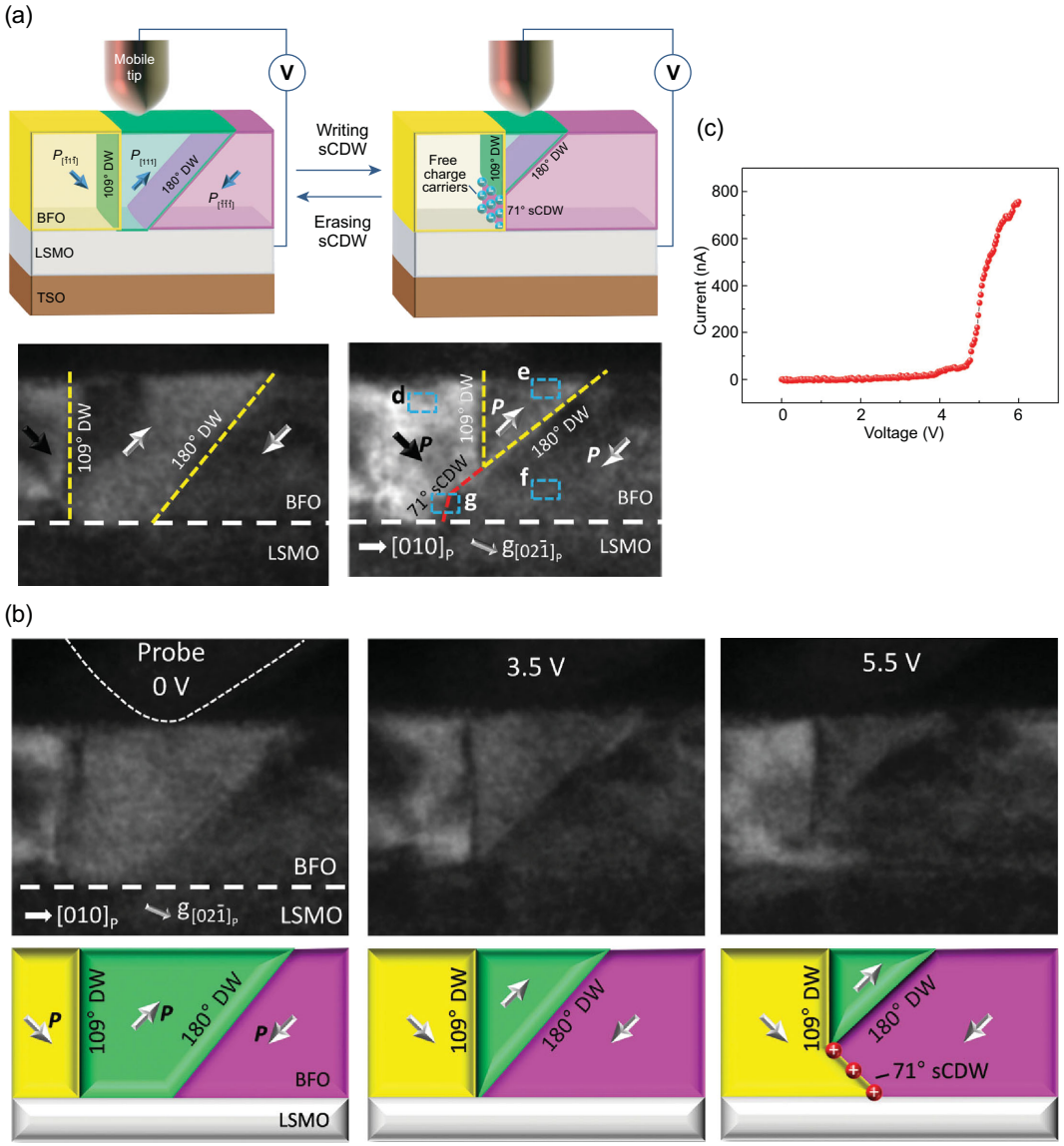

Figure 9. a) Schematic of the charged DW writing and erasing process with corresponding TEM images. b) *In-situ* switching of CDW writing. c) Corresponding *I–V* curve. Reprinted with permission from Li *et al.* [57]. Copyright (2016) WILEY-VCH Verlag GmbH & Co. KGaA, Weinheim.

which is larger than the $BiFeO_3$ bandgap. For 71° DWs, the *I–V* curves of both parallel and perpendicular geometries show significant V_{oc} of −7.6 V and − 6.6 V, respectively. Both groups' results show a V_{oc} larger than the $BiFeO_3$ bandgap, but Bhatnagar *et al.*'s work claims that the DWs, due to their relatively high intrinsic conductivity, work as resistors with lower resistance rather than working to separate charges as mentioned in Yang *et al.*'s model. The relationship between V_{oc} and the conductivity can be expressed by the following equation:

$$V_{oc} = J_{ph}\left(\frac{1}{\sigma_d + \sigma_{ph}}\right)L, \qquad [75–77]$$

where J_{ph} is the photocurrent, σ_d is the dark conductivity, σ_{ph} is the photoconductivity, and L is the distance between the electrodes. Only the dark conductivity and the photoconductivity affect V_{oc}, since J_{ph} is uniformly generated across the whole film by shift currents [78], and L is constant. In Fig. 11b, the total effective conductivity $(\sigma_d + \sigma_{ph})$ has contributions from both the domains and the DWs, which can be modeled as either a parallel or serial circuit. The perpendicular geometry gives lower V_{oc} since it has parallel conductivity mode and results in higher conductivity. Also, the 109° DW has higher conductivity than that of the 71° DW, which results in smaller V_{oc} for the 109° DW than that of 71° DWs, in all cases.

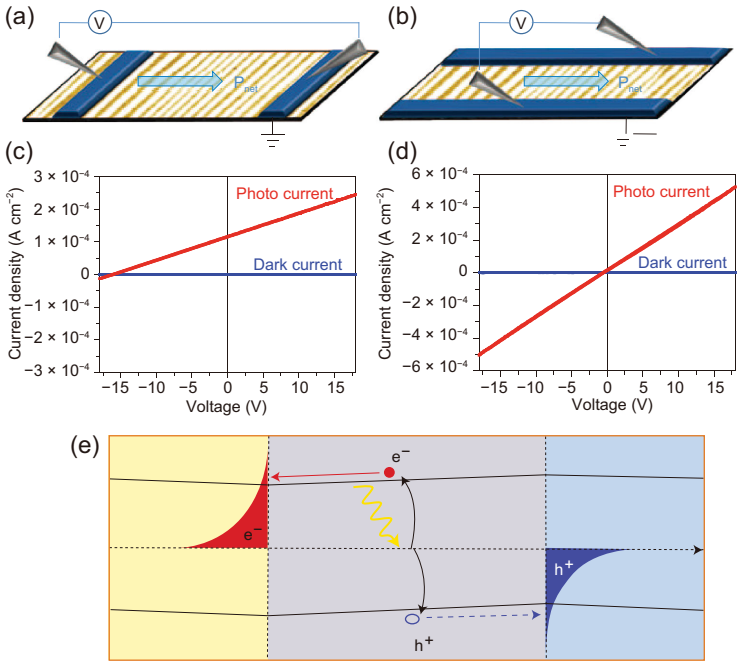

Figure 10. Geometries with electrodes (a) parallel and (b) perpendicular to the DWs and corresponding *I*–*V* curves (c) and (d). (e) The schematic of the charge separation model. Reprinted with permission from Yang *et al.* [20]. Copyright (2010) Springer Nature.

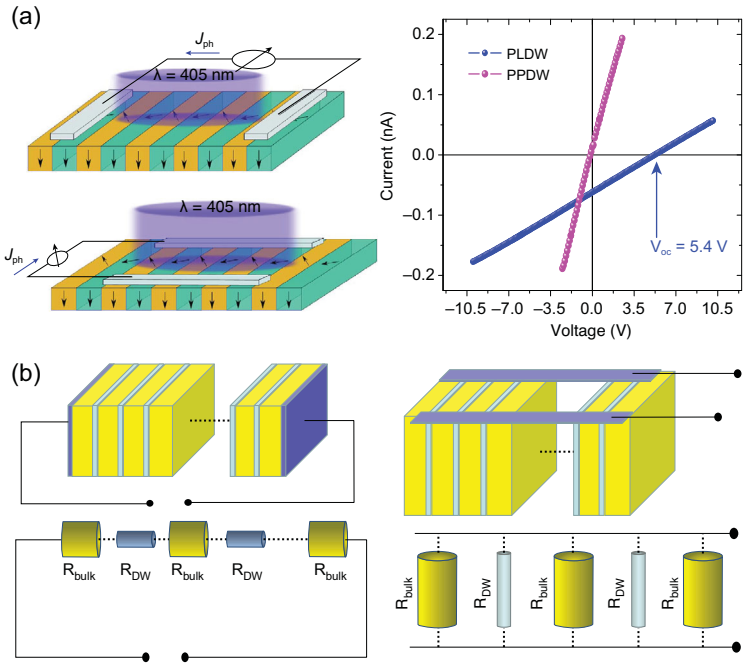

Figure 11. a) Geometries with electrodes parallel and perpendicular to the DWs and corresponding *I*–*V* curves: electrodes parallel to the DWs (PLDW) and perpendicular to the DWs (PPDW). b) A schematic of the role of the DWs. Reprinted with permission from Bhatnagar *et al.* [22]. Copyright (2013) Springer Nature.

In aggrement with Bhatnagar *et al.*'s model, Wang *et al.* reported the photovoltic effect on $BiFeO_3$ CDWs [23], which is a follow-up work to section 'Charged domain wall in a nanoisland'. They used a similar square $BiFeO_3$ nanoisland with either 'head-to-head' or 'tail-to-tail' CDWs configurations as shown in Fig. 6c and d, repectively, and photoassisted AFM to measure the photoresponse behavior [79]. As the 1.4 V bias voltage is applied, the nanoisland with 'head-to-head' CDWs shows ∼0.2 pA dark current, and 23 pA photocurrent when irradiated with a 405 nm laser, giving a photo-to-dark current on–off ratio of 11,500%. In contrast, 'tail-to-tail' CDWs show 0.69 nA dark current and 1.1 nA photocurrent, with a much lower on–off ratio of 159%. The measurements at the domains without/with laser illumination show negligible signal.

SUMMARY AND PROSPECTS

Here, we have reviewed the current status of $BiFeO_3$ DW microstructures and their conductive and photovoltaic properties. The uncharged DWs show enhanced conductance with measured current in the pA range, while the later reported CDWs have conductances of four orders of magnitude higher than the uncharged DWs. The ferroelectric switching process in CDWs opens up a way to directly manipulate their formation and motion, forming the building blocks for reconfigurable nanoelectronic devices based on writing and erasing CDWs. The role of DWs in producing photovoltaic properties is important: running parallel to the collecting electrodes provides a high open-circuit voltage larger than the $BiFeO_3$ bandgap. Many other DW properties and mechanisms are, however, still unclear and need to be explored, such as stress–polarization bound charge coupling, electron–hole pair dynamics, defect engineering with larger impurity defect dimensions, and switching processes with higher spatial resolution. To achieve this, additional characterization with TEM works is necessary.

Because of the high spatial resolution and flexibility for housing *in situ* probes, TEM has been used for studies on the atomic structure, dynamics and electronic structure of ferroelectric materials, especially heterogeneous structures such as interfaces and DWs. While unsettled mechanisms, such as point defect and oxygen vacancy dynamics, represent new challenges for characterization, the emergence of new imaging techniques may bring new possibilities to these studies. The advanced 4D STEM technique including charge density mapping may provide atomic-level local charge and electric field distribution at the DWs, giving rise

to better understanding of bound charge coupling and electron–hole pair dynamics. The cross-sectional c-AFM imaging technique [40,80] plus cross-sectional STEM provides both macro- and micro-level information that can be applied to large defect dimension studies. Vibrational microscopy and high-energy-resolution EELS, which can detect oxygen vacancies and electronic structures on the atomic scale, may help to provide more information on and better explanations for many current problems. For DW switching, only low-magnification TEM images have been available thus far because most *in situ* sample holders are limited to a single tilt axis, making it impossible to accurately align the microscope onto the crystal's zone axis, a requirement for atomic resolution imaging. The new double tilt *in situ* TEM holder developed by Mingjie Xu *et al.* [81] opens up a possible path to tilt the sample to the zone axis, enabling the acquisition of high-magnification atomic-scale switching images. This may help improve our understanding of DW formation and the interaction with surrounding defects during the process.

ACKNOWLEDGEMENTS

We thank Prof. Jun-Ming Liu for inviting us to write this review paper. We would like to acknowledge the use of the advanced TEM facilities in the Irvine Materials Research Institute (IMRI) at the University of California, Irvine.

FUNDING

This work was supported by the US Department of Energy, Office of Basic Energy Sciences, Division of Materials Sciences and Engineering under Award DE-SC0014430.

REFERENCES

1. Vonhippel A, Breckenridge RG and Chesley FG *et al.* High dielectric constant ceramics. *Ind Eng Chem* 1946; **38**: 1097–109.
2. Sergei VK, Anna NM and Long Qing C *et al.* Local polarization dynamics in ferroelectric materials. *Rep Prog Phys* 2010, **73**: 056502.
3. Ishiwara H. Ferroelectric random access memories. *J Nanosci Nanotechnol* 2012; **12**: 7619–27.
4. Streiffer SK, Parker CB and Romanov AE *et al.* Domain patterns in epitaxial rhombohedral ferroelectric films. I. Geometry and experiments. *J Appl Phys* 1998; **83**: 2742–53.
5. Chu YH, Zhan Q and Martin LW *et al.* Nanoscale domain control in multiferroic $BiFeO_3$ thin films. *Adv Mater* 2006; **18**: 2307–11.
6. De Luca G, Strkalj N and Manz S *et al.* Nanoscale design of polarization in ultrathin ferroelectric heterostructures. *Nat Commun* 2017; **8**: 1419.
7. Maksymovych P, Morozovska AN and Yu P *et al.* Tunable metallic conductance in ferroelectric nanodomains. *Nano Lett* 2012; **12**: 209–13.
8. Vasudevan RK, Morozovska AN and Eliseev EA *et al.* Domain wall geometry controls conduction in ferroelectrics. *Nano Lett* 2012; **12**: 5524–31.
9. Crassous A, Sluka T and Tagantsev AK *et al.* Polarization charge as a reconfigurable quasi-dopant in ferroelectric thin films. *Nat Nanotechnol* 2015; **10**: 614–8.
10. Solmaz A, Huijben M and Koster G *et al.* Domain selectivity in $BiFeO_3$ thin films by modified substrate termination. *Adv Funct Mater* 2016; **26**: 2882–9.
11. Paruch P, Giamarchi T and Triscone JM. Domain wall roughness in epitaxial ferroelectric $PbZr_{0.2}Ti_{0.8}O_3$ thin films. *Phys Rev Lett* 2005; **94**: 197601.
12. Lubk A, Rossell MD and Seidel J *et al.* Evidence of sharp and diffuse domain walls in $BiFeO_3$ by means of unit-cell-wise strain and polarization maps obtained with high resolution scanning transmission electron microscopy. *Phys Rev Lett* 2012; **109**: 047601.
13. Vrejoiu I, Le Rhun G and Zakharov ND *et al.* Threading dislocations in epitaxial ferroelectric $PbZr_{0.2}Ti_{0.8}O_3$ films and their effect on polarization backswitching. *Philos Mag* 2006; **86**: 4477–86.
14. Rojac T, Bencan A and Drazic G *et al.* Domain-wall conduction in ferroelectric $BiFeO_3$ controlled by accumulation of charged defects. *Nat Mater* 2017; **16**: 322–7.
15. Seidel J, Martin LW and He Q *et al.* Conduction at domain walls in oxide multiferroics. *Nat Mater* 2009; **8**: 229–34.
16. Seidel J, Maksymovych P and Batra Y *et al.* Domain wall conductivity in La-doped $BiFeO_3$. *Phys Rev Lett* 2010; **105**: 197603.
17. Farokhipoor S and Noheda B. Conduction through 71° domain walls in $BiFeO_3$ thin films. *Phys Rev Lett* 2011; **107**: 127601.
18. Sharma P, Zhang Q and Sando D *et al.* Nonvolatile ferroelectric domain wall memory. *Sci Adv* 2017; **3**: e1700512.
19. Jiang J, Bai ZL and Chen ZH *et al.* Temporary formation of highly conducting domain walls for non-destructive read-out of ferroelectric domain-wall resistance switching memories. *Nat Mater* 2018; **17**: 49–56.
20. Yang SY, Seidel J and Byrnes SJ *et al.* Above-bandgap voltages from ferroelectric photovoltaic devices. *Nat Nanotechnol* 2010; **5**: 143–7.
21. Alexe M and Hesse D. Tip-enhanced photovoltaic effects in bismuth ferrite. *Nat Commun* 2011; **2**: 256.
22. Bhatnagar A, Roy Chaudhuri A and Heon Kim Y *et al.* Role of domain walls in the abnormal photovoltaic effect in $BiFeO_3$. *Nat Commun* 2013; **4**: 2835.
23. Wang J, Ma J and Yang Y *et al.* Ferroelectric photodetector with high current on–off ratio (~1 × 104%) in self-assembled topological nanoislands. *ACS Appl Electron Mater* 2019; **1**: 862–8.
24. Wang F, Young SM and Zheng F *et al.* Substantial bulk photovoltaic effect enhancement via nanolayering. *Nat Commun* 2016; **7**: 10419.
25. Inoue R, Ishikawa S and Imura R *et al.* Giant photovoltaic effect of ferroelectric domain walls in perovskite single crystals. *Sci Rep* 2015; **5**: 14741.

26. Chu K, Jang B-K and Sung JH *et al.* Enhancement of the anisotropic photocurrent in ferroelectric oxides by strain gradients. *Nat Nanotechnol* 2015; **10**: 972–9.
27. Schaab J, Skjærvø SH and Krohns S *et al.* Electrical half-wave rectification at ferroelectric domain walls. *Nat Nanotechnol* 2018; **13**: 1028–34.
28. Zavaliche F, Yang SY and Zhao T *et al.* Multiferroic $BiFeO_3$ films: domain structure and polarization dynamics. *Phase Transitions* 2006; **79**: 991–1017.
29. Zeches RJ, Rossell MD and Zhang JX *et al.* A strain-driven morphotropic phase boundary in $BiFeO_3$. *Science* 2009; **326**: 977–80.
30. Christen HM, Nam JH and Kim HS *et al.* Stress-induced R-MA-MC-T symmetry changes in $BiFeO_3$ films. *Phys Rev B* 2011; **83**: 144107.
31. Li LZ, Zhang Y and Xie L *et al.* Atomic-scale mechanisms of defect-induced retention failure in ferroelectrics. *Nano Lett* 2017; **17**: 3556–62.
32. Nelson CT, Winchester B and Zhang Y *et al.* Spontaneous vortex nanodomain arrays at ferroelectric heterointerfaces. *Nano Lett* 2011; **11**: 828–34.
33. Yun KY, Ricinschi D and Kanashima T *et al.* Giant ferroelectric polarization beyond 150 $\mu C/cm^2$ in $BiFeO_3$ thin film. *Jpn J Appl Phys* 2004; **43**: L647–8.
34. Wang J, Neaton JB and Zheng H *et al.* Epitaxial $BiFeO_3$ multiferroic thin film heterostructures. *Science* 2003; **299**: 1719–22.
35. Vasudevan RK, Chen Y-C and Tai H-H *et al.* Exploring topological defects in epitaxial $BiFeO_3$ thin films. *ACS Nano* 2011; **5**: 879–87.
36. Yadav AK, Nelson CT and Hsu SL *et al.* Observation of polar vortices in oxide superlattices. *Nature* 2016; **530**: 198–201.
37. Schlom DG, Chen L-Q and Eom C-B *et al.* Strain tuning of ferroelectric thin films. *Annu Rev Mater Res* 2007; **37**: 589–626.
38. Schlom DG, Chen L-Q and Pan X *et al.* A thin film approach to engineering functionality into oxides. *J Am Ceram Soc* 2008; **91**: 2429–54.
39. Martin LW, Chu YH and Ramesh R. Advances in the growth and characterization of magnetic, ferroelectric, and multiferroic oxide thin films. *Mater Sci Eng R Rep* 2010; **68**: 89–133.
40. Li L, Jokisaari JR and Zhang Y *et al.* Control of domain structures in multiferroic thin films through defect engineering. *Adv Mater* 2018; **30**: 1802737.
41. Li L, Cheng X and Jokisaari JR *et al.* Defect-induced hedgehog polarization states in multiferroics. *Phys Rev Lett* 2018; **120**: 137602.
42. Chen Z, Liu J and Qi Y *et al.* 180° ferroelectric stripe nanodomains in $BiFeO_3$ thin films. *Nano Lett* 2015; **15**: 6506–13.
43. Choi KJ, Biegalski M and Li YL *et al.* Enhancement of ferroelectricity in strained $BaTiO_3$ thin films. *Science* 2004; **306**: 1005–9.
44. Ederer C and Spaldin NA. Effect of epitaxial strain on the spontaneous polarization of thin film ferroelectrics. *Phys Rev Lett* 2005; **95**: 257601.
45. Schlom D, Gv Chen L-Q and Fennie CJ *et al.* Elastic strain engineering of ferroic oxides. *MRS Bull* 2014; **39**: 118–30.
46. Adamo C, Ke X and Wang HQ *et al.* Effect of biaxial strain on the electrical and magnetic properties of (001) $La_{0.7}Sr_{0.3}MnO_3$ thin films. *Appl Phys Lett* 2009; **95**: 112504.
47. Infante IC, Lisenkov S and Dupe B *et al.* Bridging multiferroic phase transitions by epitaxial strain in $BiFeO_3$. *Phys Rev Lett* 2010; **105**: 057601.
48. Bea H, Dupe B and Fusil S *et al.* Evidence for room-temperature multiferroicity in a compound with a giant axial ratio. *Phys Rev Lett* 2009; **102**: 217603.
49. Chisholm MF, Luo WD and Oxley MP *et al.* Atomic-scale compensation phenomena at polar interfaces. *Phys Rev Lett* 2010; **105**: 197602.
50. Lichtensteiger C, Fernandez-Pena S and Weymann C *et al.* Tuning of the depolarization field and nanodomain structure in ferroelectric thin films. *Nano Lett* 2014; **14**: 4205–11.
51. Li YL, Hu SY and Liu ZK *et al.* Effect of electrical boundary conditions on ferroelectric domain structures in thin films. *Appl Phys Lett* 2002; **81**: 427–9.
52. Chu YH, Cruz MP and Yang CH *et al.* Domain control in multiferroic $BiFeO_3$ through substrate vicinality. *Adv Mater* 2007; **19**: 2662–6.
53. Jang HW, Ortiz D and Baek SH *et al.* Domain engineering for enhanced ferroelectric properties of epitaxial (001) $BiFeO_3$ thin films. *Adv Mater* 2009; **21**: 817–23.
54. Folkman CM, Baek SH and Jang HW *et al.* Stripe domain structure in epitaxial (001) $BiFeO_3$ thin films on orthorhombic $TbScO_3$ substrate. *Appl Phys Lett* 2009; **94**: 251911.
55. Chu Y-H, He Q and Yang C-H *et al.* Nanoscale control of domain architectures in $BiFeO_3$ thin films. *Nano Lett* 2009; **9**: 1726–30.
56. Li LZ, Gao P and Nelson CT *et al.* Atomic scale structure changes induced by charged domain walls in ferroelectric materials. *Nano Lett* 2013; **13**: 5218–23.
57. Li LZ, Britson J and Jokisaari JR *et al.* Giant resistive switching via control of ferroelectric charged domain walls. *Adv Mater* 2016; **28**: 6574–80.
58. Nesterov O, Matzen S and Magen C *et al.* Thickness scaling of ferroelastic domains in $PbTiO_3$ films on $DyScO_3$. *Appl Phys Lett* 2013; **103**: 142901.
59. Catalan G, Janssens A and Rispens G *et al.* Polar domains in lead titanate films under tensile strain. *Phys Rev Lett* 2006; **96**: 127602.
60. Tang YL, Zhu YL and Ma XL *et al.* Observation of a periodic array of flux-closure quadrants in strained ferroelectric $PbTiO_3$ films. *Science* 2015; **348**: 547–51.
61. Liu Y, Wang Y-J and Zhu Y-L *et al.* Large scale two-dimensional flux-closure domain arrays in oxide multilayers and their controlled growth. *Nano Lett* 2017; **17**: 7258–66.
62. Li S, Wang YJ and Zhu YL *et al.* Evolution of flux-closure domain arrays in oxide multilayers with misfit strain. *Acta Mater* 2019; **171**: 176–83.
63. Gao P, Nelson CT and Jokisaari JR *et al.* Direct observations of retention failure in ferroelectric memories. *Adv Mater* 2012; **24**: 1106–10.
64. Sluka T, Tagantsev AK and Bednyakov P *et al.* Free-electron gas at charged domain walls in insulating $BaTiO_3$. *Nat Commun* 2013; **4**: 1808.
65. Vul BM, Guro GM and Ivanchik II. Encountering domains in ferroelectrics. *Ferroelectrics* 1973; **6**: 29–31.
66. Gureev MY, Tagantsev AK and Setter N. Head-to-head and tail-to-tail 180° domain walls in an isolated ferroelectric. *Phys Rev B* 2011; **83**: 184104.
67. Bednyakov PS, Sluka T and Tagantsev AK *et al.* Formation of charged ferroelectric domain walls with controlled periodicity. *Sci Rep* 2015; **5**: 15819.
68. Li L, Britson J and Jokisaari JR *et al.* Giant resistive switching via control of ferroelectric charged domain walls. *Adv Mater* 2016; **28**: 6574–80.
69. Ma J, Ma J and Zhang Q *et al.* Controllable conductive readout in self-assembled, topologically confined ferroelectric domain walls. *Nat Nanotechnol* 2018; **13**: 947–52.
70. Nelson CT, Gao P and Jokisaari JR *et al.* Domain dynamics during ferroelectric switching. *Science* 2011; **334**: 968–71.
71. Balke N, Choudhury S and Jesse S *et al.* Deterministic control of ferroelastic switching in multiferroic materials. *Nat Nanotechnol* 2009; **4**: 868–75.
72. Gur I, Fromer NA and Geier ML *et al.* Air-stable all-inorganic nanocrystal solar cells processed from solution. *Science* 2005; **310**: 462–5.
73. O'Regan B and Grätzel M. A low-cost, high-efficiency solar cell based on dye-sensitized colloidal TiO_2 films. *Nature* 1991; **353**: 737–40.
74. Basu SR, Martin LW and Chu YH *et al.* Photoconductivity in $BiFeO_3$ thin films. *Appl Phys Lett* 2008; **92**: 091905.
75. Chynoweth AG. Surface space-charge layers in barium titanate. *Phys Rev* 1956; **102**: 705–14.
76. Ruppel W, Von Baltz R and Wurfel P. The origin of the photo-emf in ferroelectric and non-ferroelectric materials. *Ferroelectrics* 1982; **43**: 109–23.

77. Fridkin VM. *Photoferroelectrics*. Berlin Heidelberg: Springer-Verlag, 1979.
78. Young SM, Zheng F and Rappe AM. First-principles calculation of the bulk photovoltaic effect in bismuth ferrite. *Phys Rev Lett* 2012; **109**: 236601.
79. Wang J, Huang H and He W *et al*. Nanoscale bandgap tuning across an inhomogeneous ferroelectric interface. *ACS Appl Mater Interfaces* 2017; **9**: 24704–10.
80. Zhang Y, Lu H and Xie L *et al*. Anisotropic polarization-induced conductance at a ferroelectric–insulator interface. *Nat Nanotechnol* 2018; **13**: 1132–6.
81. Xu M, Dai S and Blum T *et al*. Double-tilt in situ TEM holder with ultra-high stability. *Ultramicroscopy* 2018; **192**: 1–6.